AIAA SciTech
4-8 January 2016, San Diego, California, USA
54th AIAA Aerospace Sciences Meeting

Instability and Transition Experiments in the Boeing/AFOSR Mach 6 Quiet Tunnel

Cameron J. Sweeney*, Brandon C. Chynoweth*, Josh B. Edelman*,
and Steven P. Schneider†
School of Aeronautics and Astronautics
Purdue University
West Lafayette, IN 47907-1282

This paper presents results for two projects in the Boeing/AFOSR Mach 6 Quiet Tunnel (BAM6QT) at Purdue University.

1. **A parametric study using RIM roughness inserts was performed on a flared cone geometry to determine the effect of roughness height on the growth and breakdown of second-mode waves. As the roughness height decreased, the maximum magnitude of the pressure fluctuations due to the second-mode reached nearly 25%. An adjustable angle-of-attack adapter was tested. Performing angle-of-attack adjustments of less than 1° is now possible.**
2. **Secondary instabilities of the hypersonic stationary crossflow wave were measured on a 7° half-angle right circular cone at 6° angle of attack. The measured frequencies indicate the presence of multiple secondary instability modes, and compare well to an estimate based on the edge velocity and boundary layer thickness. The instabilities were measured from about 110° to 160° from the windward ray over a wide range of Reynolds numbers. The group velocity of the instabilities is close to the local the edge velocity. The maximum pressure fluctuation of the instabilities before breakdown was around 20-25% of the local edge pressure for the two instabilities whose full development was measured.**

Nomenclature

f	frequency	x	model axial coordinate
M	Mach number	r	model radial coordinate
p	pressure	θ	azimuthal angle
$\dot{q}$	heat flux	k	roughness height
Re	Reynolds number	δ	boundary layer thickness
T	Temperature	A	amplitude
t	time	A_0	initial amplitude
τ	time delay		
Θ	phase difference		

*Research Assistant. Student Member, AIAA
†Professor. Associate Fellow, AIAA

Subscripts

0	stagnation condition
e	boundary layer edge condition
∞	freestream condition

Abbreviations

BAM6QT	Boeing/AFOSR Mach-6 Quiet Tunnel
TSP	Temperature-Sensitive Paint
PSD	Power-Spectral Density
RIM	Rod Insertion Method
STABL	Stability and Transition Analysis for Hypersonic Bounda

I. Introduction

A. Hypersonic Laminar-Turbulent Transition

Accurately predicting the boundary-layer transition location during hypersonic flight is critical for determining many key aerodynamic properties including skin friction, heat transfer, and separation.[1] For example, the heat transfer associated with a turbulent boundary layer is typically 3-5 times greater than that of a laminar boundary layer during hypersonic flow.[2] The difference in heat transfer can lead to significant differences in vehicle design depending on which locations on the vehicle experience a turbulent boundary layer. Without a thorough understanding of hypersonic boundary-layer transition, efficient design of hypersonic vehicles can be difficult. Conservative vehicle design could result in a vehicle that has over-designed features, adding superfluous costs and weight. Alternatively, less conservative vehicle design could result in under-designed features which could ultimately lead to vehicle failure.

Hypersonic boundary-layer transition is not a well understood process. Transition typically occurs when disturbances enter the boundary layer and grow. Many factors play a role in determining when the instabilities become large enough to cause transition. Some of the most significant factors are Reynolds number, Mach number, surface roughness, freestream vorticity, and noise levels. Though not always the largest fluctuation in flight, acoustic noise has traditionally been the primary freestream fluctuation present in hypersonic wind tunnels.[1] Conventional hypersonic wind tunnels typically have much higher noise levels than are present in flight conditions. Quiet wind tunnels allow for the study of transition mechanisms in a low noise environment, comparable to those found in flight.

B. The Boeing/AFOSR Mach-6 Quiet Tunnel

The Boeing/AFOSR Mach-6 Quiet Tunnel (BAM6QT), located at Purdue University, is a hypersonic low-disturbance wind tunnel capable of achieving freestream noise levels as low as 0.01%.[3] The BAM6QT, shown in in Figure 1, is a Ludweig tube design which utilizes two regions separated by diaphragms. The upstream region consists of a long driver tube, including a converging-diverging nozzle, and the downstream region consists of a large dump tank. The first region is filled to the desired pressure with highly filtered air while the dump tank is simultaneously pumped down to near vacuum. To start a run the diaphragms burst via manipulating the pressure maintained between them. When the diaphragms burst an expansion wave travels upstream through the nozzle and a shock wave travels downstream. Mach 6 flow is obtained when the expansion wave passes through the nozzle. The expansion wave then continues to propagate upstream until it reaches the end of the driver tube, where it then reflects off the end wall. The expansion waves continues to reflect back and forth in the driver tube, causing a quasi-static drop in the total pressure during a run.

Through the use of three key features, the BAM6QT is able to maintain noise levels as low as 0.01% for stagnation pressures up to 170 psia. Firstly, the nozzle is fitted with a suction slot that bleeds the boundary layer away entering the nozzle, leaving a fresh laminar boundary layer along the nozzle. Secondly, the nozzle is polished to a mirror finish to minimize effects of surface roughness on the boundary layer of the nozzle. Finally, the diverging section of the nozzle is elongated to limit the growth of the Görtler instability. In addition to its quiet flow capabilities, if the fast-valve bleed suction is turned off the BAM6QT is able to operate as a conventional tunnel with noise levels around 3%.[3]

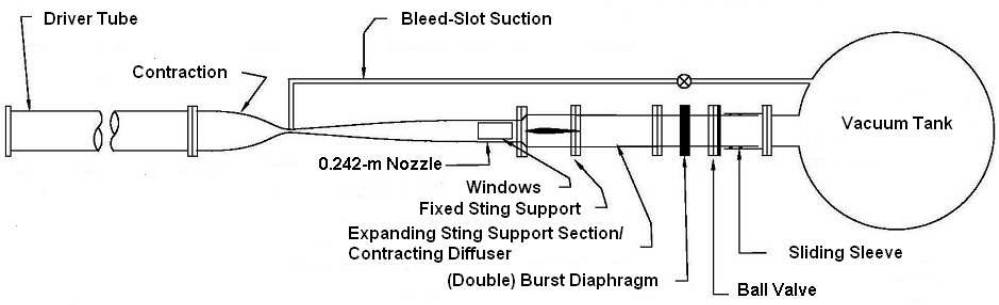

Figure 1. Schematic of Boeing/AFOSR Mach 6 Quiet Tunnel.

II. Transition Measurements on a Flared Cone Geometry

A. Model and Instrumentation

At Mach 6 the transition process on axisymmetric geometries at zero degrees angle of attack is dominated by the second-mode instability. Since the frequency of the second-mode wave is tuned to the boundary layer thickness, a flared cone model was designed to maintain a nearly constant boundary layer thickness by Wheaton.[4] The constant boundary-layer thickness amplifies a small band of second-mode frequencies over a large spatial extent that allows for measurements of the growth, saturation, and breakdown leading to laminar-turbulent transition.

All experiments were performed on a flared cone with a constant 3-meter circular arc. The model consists of a nosetip, a roughness insert, and a frustum as shown in Figure 2. This model is referred to as the Roughness Insert Cone. The total model length is 51.7 cm with a base diameter of 11.4 cm (4.5 inches). The nosetip is 25.4 cm long with a nose radius of 152 μm (0.006 inches) and an opening half-angle of approximately 1.5°. The cone was designed with a space 0.635 cm (0.25 inches) wide between the nosetip and the frustum. This gap is filled with a removable roughness insert that can either be left unmodified to test smooth wall cases, or roughness elements can be added to the surface creating a RIM roughness, Figure 3, previously reported on by Chynoweth.[5] The insert allows for testing of both destructive and non-destructive methods of producing roughnesses. Sensors are placed along a single ray at a distance of 33.9, 36.5, 39.0, 41.6, 44.1, 46.6, and 49.2 cm from the nosetip. Three additional sensor holes were added +/- 90° and 180° from the main sensor ray at 46.6 cm from the nosetip to facilitate the use of the adjustable angle-of-attack adapter which will be discussed in Section C.

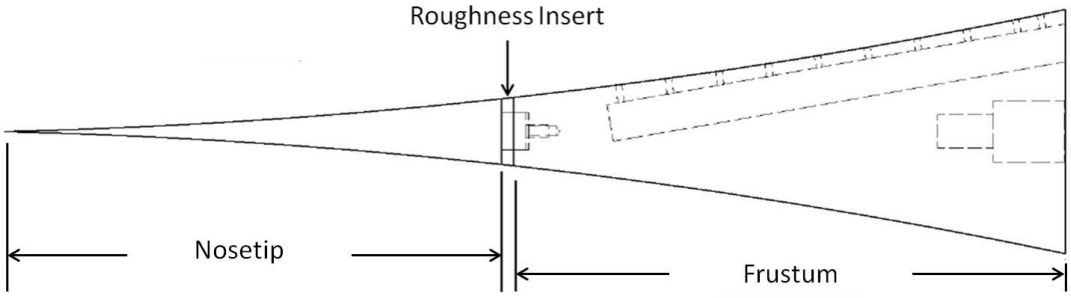

Figure 2. Schematic of the roughness insert cone with a 11.4 cm base diameter.

The mean flow around the model was computed using the Stability and Transition Analysis for Hypersonic Boundary Layers (STABL) code developed at the University of Minnesota. A grid was generated for both the

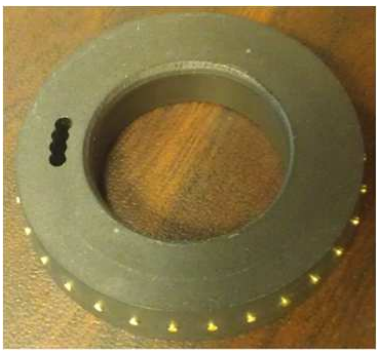

Figure 3. Photograph of a RIM insert. The insert is made of Torlon with brass rods inserted every 12° as roughness elements.

4-inch base cone and the Roughness Insert Cone. The ratio of the surface static pressure to the freestream stagnation pressure was computed for stagnation pressures of 90, 120, 140, and 160 psia. Across this 70 psia range, the ratio at any given stagnation pressure was less than 1% different than the mean value. Therefore, the average of ratio from the four computations was used to calculate pressure ratio on the surface at each discrete sensor location and used in normalization when computing the power spectral densities. More detail can be found in the Master's Thesis of Chynoweth.[6]

B. A Study on the Effect of RIM Roughness Heights

All RIM inserts tested had 30 evenly spaced elements with each having a diameter of approximately 840 μm. For any one insert, all of the roughness heights (k) are identical. Eight different RIM inserts were fabricated with heights varying from k = 0.020" (510 μm) to k = 0.006" (150 μm) in 0.002" (50 μm) increments. In the following experiments, the "smooth wall" condition refers to experiments performed with an insert devoid of any roughness elements. Based on previous experiments, all data were obtained at a unit Re = 10.1 $\pm$ 0.1×10^6/m for optimal visualization using temperature sensitive paint (TSP).

Figure 4 shows TSP data near the main sensor ray for all roughnesses tested as well as the smooth wall condition with flow occurring from right to left. The same portion of the full TSP image was extracted and aligned to facilitate comparisons. The heat transfer averaged azimuthally across the field of view is shown in Figure 5. Two anomalies caused by experimental error will first be discussed, followed by a review of the results.

For the smooth wall, k = 0.008", and k = 0.012" cases, the streaks near 40 cm from the nosetip occur up to 5 cm further upstream on the lower portion of each image than on the top. This is due to a slight misalignment of the model to the incoming flow, causing a non-zero angle of attack. A perceived increase in heat transfer is seen for the k = 0.010" experiment. This is caused by the Schmidt-Boelter gauge being directly beneath a region of increased heating creating large uncertainties in the TSP calibration process. For future tests the Schmidt-Boelter gauge will be placed further upstream on the model surface.

It can be seen that for the smooth wall, a set of streaks with an azimuthal wavenumber of approximately 90 begins to form near 39.0 cm from the nosetip. At 41.6 cm, the heating decreases until 46.6 cm from the nosetip where a second increase in heating is observed. As the roughness height is increased to k = 0.006", 0.008", and 0.010", a pair of streaks forms directly downstream from each element starting at x = 39.0 cm. In between the pairs of streaks, a single streak forms near 41.5 cm. The average heat transfer across the field of view, Figure 5, shows that a peak in heating occurs near x = 40 cm for all cases up to k = 0.010". Increasing the height to k = 0.012" and 0.014", only a single streak is observed behind each element instead of a streak pair. A peak in the average azimuthal heat transfer no longer occurs 40 cm from the nosetip. Further increasing the roughness element heights causes a pair of streaks that dominate the heating pattern completely eliminating any other streak phenomenon previously observed at x = 40 cm.

For the PCB sensors along the main sensor ray, pressure fluctuation magnitudes were computer for 16 different times during each run. The magnitudes can be seen in Figure 6. For roughness heights of k = 0.016" and greater, a peak in the fluctuations is not observed. As the height was decreased from 0.014" down to 0.006", the maximum magnitude increases from approximately 16% to 24%. Due to the placement of the Schmidt-Boelter gauge, there is a large gap in the pressure magnitude data causing uncertainty in whether the actual peak fluctuation had been measured. For future tests, the Schmidt-Boelter gauge will be placed in a different position to eliminate this gap.

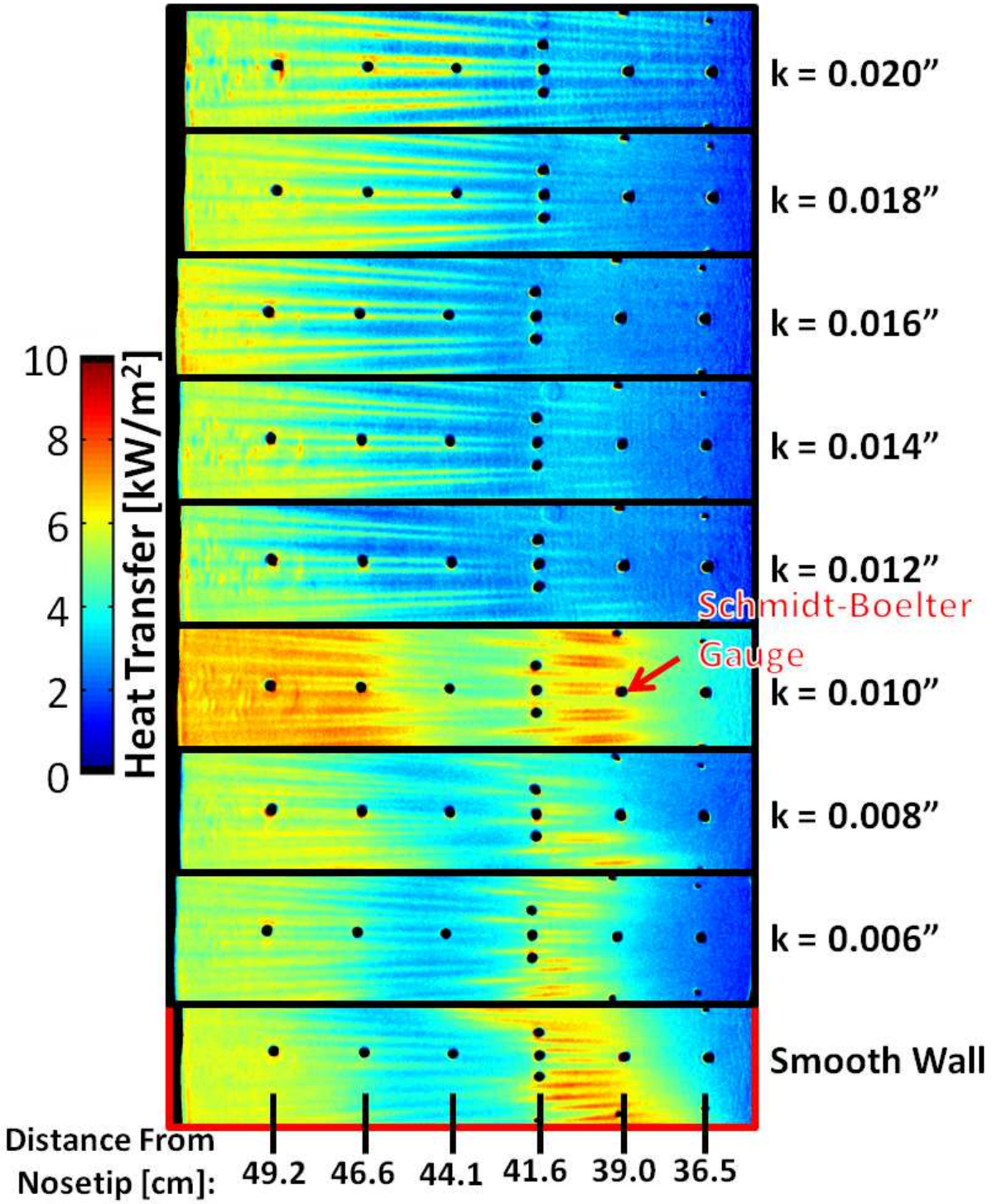

Figure 4. TSP image near main sensor ray showing effect of roughness height on observed heating patterns. Unit Re $\approx 10.1\times10^6$/m , flow is from right to left.

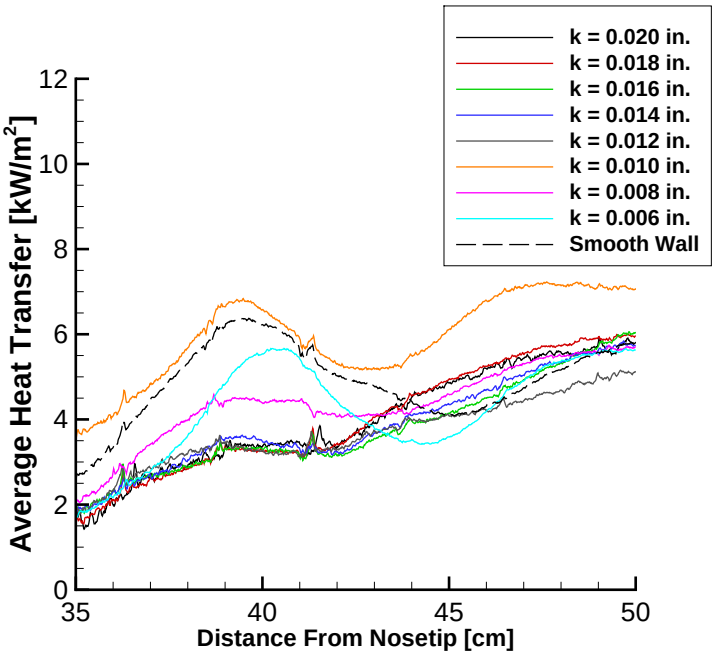

Figure 5. Heat transfer rate averaged azimuthally across the field of view showing distinct change between k = 0.014" and k = 0.010". Peak at k = 0.008" may not be observed due to model being at a slight angle of attack.

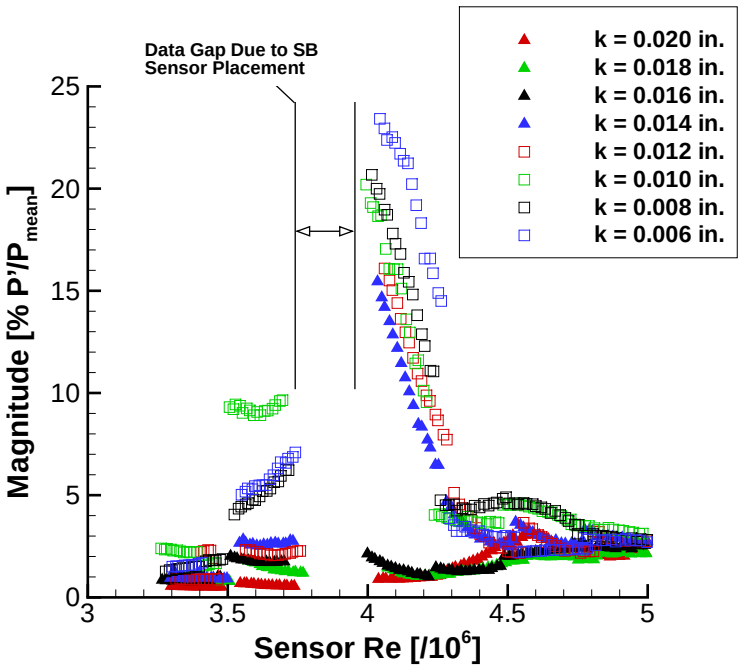

Figure 6. Power spectral density for PCB sensor 41.6 cm from the nosetip showing a distinct change when the roughness height is increased from k = 0.014" to 0.016".

C. Preliminary Results Using Adjustable Angle-of-Attack Adapter

Experiments performed by Sebastian Willems on a 3° half-angle straight cone in the BAM6QT showed that small angle-of-attack adjustments could be made using a specially designed sting.[7] Using four PCB sensors spaced 90° apart azimuthally, it is possible to determine the second-mode instability frequency on opposite sides of an axisymmetric model. A higher frequency indicates a thinner boundary layer(normally indicative of the windward side) while a lower frequency indicates a thicker boundary layer (normally seen on the leeward side of a model). When the same peak frequency is measured on all four sensors simultaneously, the model should be nominally at 0° angle of attack.

Using drawings provided by Sebastian Willems, a similar angle-of-attack adapter was designed and fabricated at Purdue University. A photograph of the adapter is shown in Figure 7. By turning the screws on opposite sides of the adapter, small adjustments to the angle of attack can be achieved. Since the screws are 3/8 x 24, one full turn changes the angle by approximately 0.36°. With the four screws, the model can be adjusted in two different planes. For the results presented, movements of the nosetip in the vertical direction are referred to as pitch adjustments. Moving the nosetip horizontally away or towards the camera are termed yaw adjustments.

Figure 7. Photograph of adjustable angle-of-attack adapter. Metal rod in lower half of photograph holds the model and inserted into upper piece.

All data for angle-of-attack adjustments were collected at a unit Re = 7.4 ± 0.2×10^6/m. While the adjustment was successful, several different problems arose that will need to be addressed when testing with the adjustable adapter in the future. First, nozzle wall boundary-layer separation was observed at this unit Reynolds number when testing with the Roughness Insert Cone. Due to the separation, one second or less of usable data was collected during each run. A result of the reduced amount of data is that the TSP images could not be converted to global heat transfer. Only images with the temperature change based off of the ratio of pixel intensities will be presented in this section. Additionally, the azimuthally spaced sensors were located in the region where streaks of increased heating occur. It is unknown how this may affect the results, but future testing should have sensors placed further upstream where no streak of increased heating are observed.

The model was initially installed in the BAM6QT facility without any adjustment to the adapter, so the model was at an unknown angle of attack. The TSP image in Figure 8 shows that the streaks are not azimuthally uniform. The PSD of the four azimuthally spaced sensors was computed and is shown in Figure 9. The double peak of the PCB sensor on the main ray has never been observed before. The sharp peak at 250 kHz was calculated for all four sensors, but the cause is unknown. When determining the peak second-mode frequency this sharp peak was not used. The table accompanying Figure 9 shows that the frequency on the main sensor ray is 45 kHz lower than sensor at 180°, and the sensor at -90° measures a peak frequency about 20 kHz lower than the sensor at +90°.

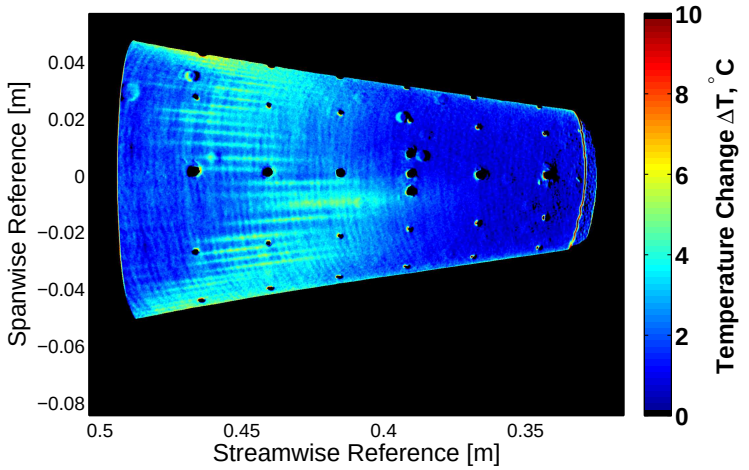

Figure 8. TSP image of model prior to any angle-of-attack adjustments. Quiet flow, unit Re ≈ 7.3×10^6/m. Flow is from right to left.

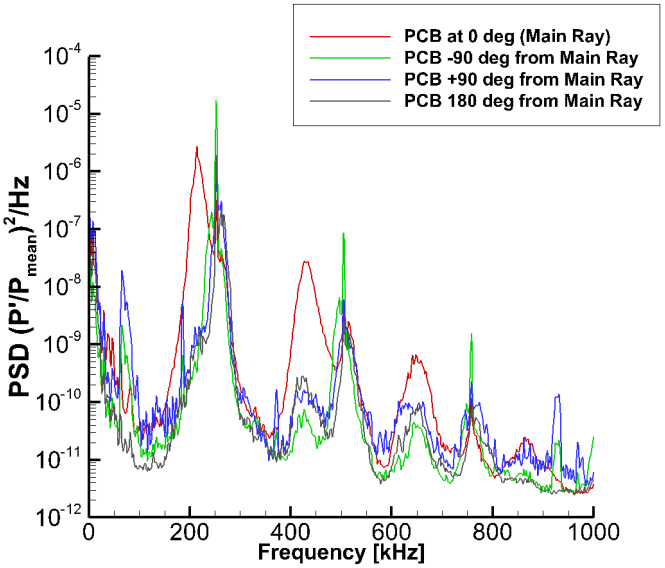

PCB Location	Peak Frequency [kHz]
0°	214
+180°	260
+90°	262
-90°	244

Figure 9. PSD from the four azimuthally spaced sensor at the same instant as the TSP image in Figure 8.

The model was pitched upwards by a 1/4 turn of the bolt (≈0.1°) and yawed away from the camera by a 1/2 turn of the bolt (≈0.2°). The TSP image in Figure 10 shows that the front of the streaks is more azimuthally uniform than in Figure 8. Figure 11 shows the PSD of each sensor as well as the peak second-mode frequencies. The PCB sensors at +90° and -90° now both have a peak frequency of 250 kHz, and the frequency on the main ray is now 12 kHz lower than the PCB on the opposite side. The double peak of the sensor on the main ray is no longer observed.

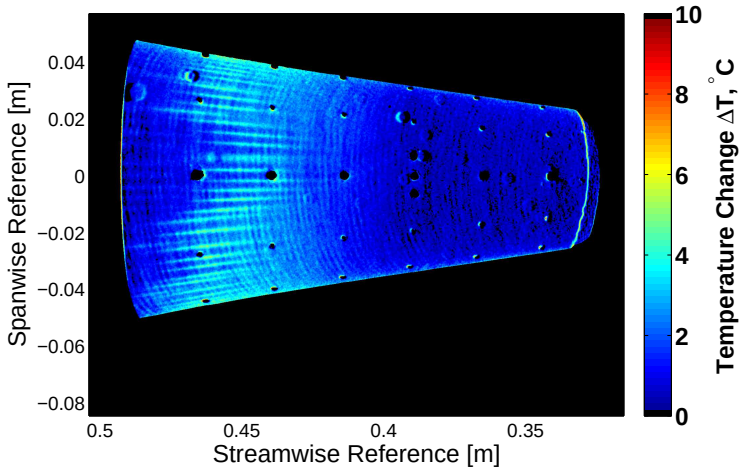

Figure 10. TSP image after first set of adjustments showing improvement in the azimuthal uniformity of the streaks of increased heating. Quiet flow, unit Re ≈ 7.4×10^6/m. Flow is from right to left.

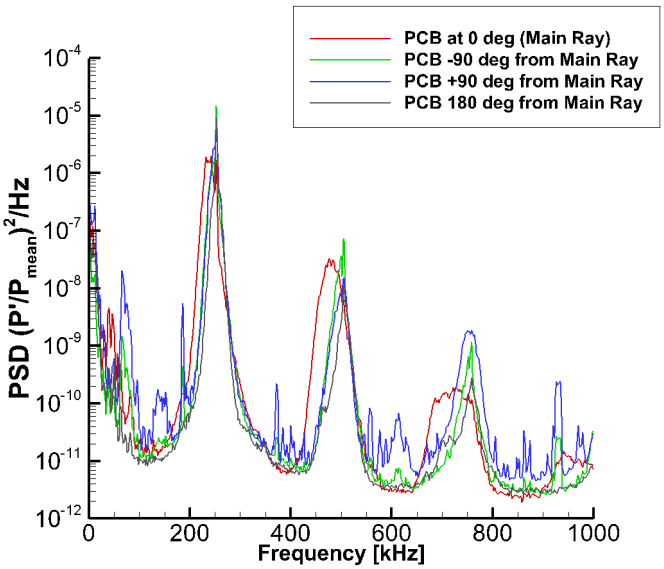

PCB Location	Peak Frequency [kHz]
0°	240
+180°	252
+90°	250
-90°	250

Figure 11. PSD from the four azimuthally spaced sensor at the same instant as the TSP image in Figure 10.

Since the peak frequencies on the ±90° sensors were identical, the model was only yawed away from the camera by 1/6 of a bolt turn (≈0.05°) to determine if a very fine adjustment could reconcile the 12 kHz difference. No apparent change is seen in the TSP image, Figure 12. The PSD's in Figure 13 show that the peak frequency measured on all four sensors is 250 ± 4 kHz. While these results show that aligning the model is possible with the new adapter, further testing is required to refine the process. Moving the PCB sensors further upstream on the surface of the model into a position where there are no streaks passing over them will eliminate any effect the streaks may have.

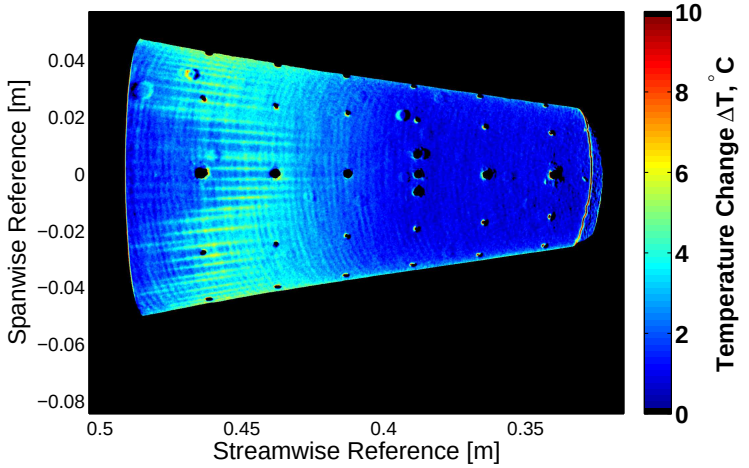

Figure 12. TSP image of model after small adjustment showing no major change in the azimuthal uniformity of the streaks of increased heating. Quiet flow, unit Re ≈ 7.5×10^6/m. Flow is from right to left.

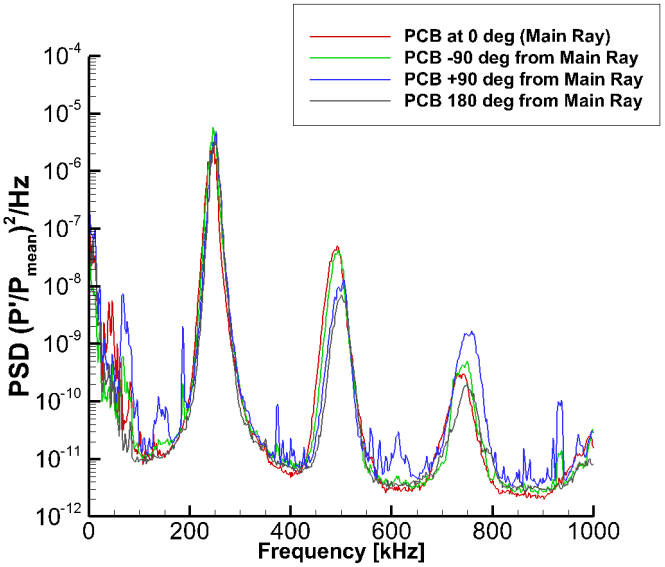

PCB Location	Peak Frequency [kHz]
0°	246
+180°	250
+90°	252
-90°	246

Figure 13. PSD from the four azimuthally spaced sensor at the same instant as the TSP image in Figure 12.

III. Secondary Instabilities of the Hypersonic Stationary Crossflow Wave

A. Introduction

On a sharp cone at angle of attack in hypersonic flow, the shock is stronger near the windward ray than toward the leeward ray. This creates a circumferential pressure gradient from the wind side to the lee side, driving a crossflow component of the boundary layer, which is unstable. The crossflow instability manifests as either a stationary vortex or travelling vortices. In the low-freestream-noise environment of the BAM6QT, the stationary mode dominates the transition process.

One path to turbulence is through secondary instabilities of the stationary vortices. These have been well studied for low-speed flows mostly on swept-wings,[8–10] and are beginning to be observed at high-speeds on sharp cones.[11,12] At low speeds a transition correlation based on N-factors of the secondary instabilities yields better results than those based on the stationary crossflow wave growth.[9] If this remains true at high speeds and a transition prediction criterion can be formed from high-speed secondary instability data, it would be a valuable tool for designers of hypersonic vehicles.

The goals of the present experiment are to determine if the instability measured by Ward and Henderson is the secondary instability of the crossflow wave;[12] to measure its properties; and to aid in the development of a transition prediction criteria based on the measured instability growth rates.

B. Model and Instrumentation

Two models were used in the present experiment, each a seven degree half-angle cone. The McKenzie-Ward (MW) cone was designed to measure secondary instabilities near the aft of the model. A schematic of the MW cone is provided in Figure 14(a). Preliminary data captured using this cone was presented in 2015.[13] The base frustum is aluminum, with a dimpled Torlon roughness insert and a stainless-steel nosetip. The total length of the McKenzie-Ward cone is about 0.4 m (16 in), with a base diameter of 0.1 m (3.92 in). Two spanwise rows of PCB 132A31 fast pressure sensors, each with four PCBs space 6° apart, were placed at 0.37 m (14.5 in) and 0.38 m (15 in) from the nosetip. A Medtherm Schmidt-Boelter gauge was placed upstream at 0.27 m (10.8 in) for TSP heat transfer reduction. The nosetip is nominally sharp with a nose radius of about 80 μm (3.2 mils).

The Streamline cone incorporates several changes to the MW cone to make more refined and consistent measurements. A schematic of this cone is provided in Figure 14(b). The base frustum is slightly longer and with a wider base, giving a total cone length of 0.41 m (16.3 in). The new cone uses the same nosetip and can use the same roughness inserts as the McKenzie-Ward cone. In addition, the new cone can use RIM inserts, modeled after those of Chynoweth,[6] which may allow more consistent roughness placement. An indexing base was added to the Streamline cone to provide better accuracy of the azimuthal orientation of the cone. The accuracy with the new base is estimated as $\pm 1°$. The sensor array consists of four streamwise rows of three PCBs, with an additional two PCBs upstream of the first row. Each row of PCBs is oriented roughly along the experimentally determined trajectory of the stationary vortices in the region 120° to 150° from the windward ray. The PCB axial locations range from 0.31 m to 0.38 m (12.2-15 in) from the nosetip. Each streamwise row is offset 6° toward the wind ray from the previous row.

The PCB data from both cones were sampled at 5 MHz. The power spectral densities and coherences were calculated using Welch's method with a frequency resolution of 2500 Hz and an overlap of 50%, unless otherwise noted. A CFD solution of the laminar flow was calculated using US3D. The pressure data is normalized by the CFD edge pressure at the same azimuthal location as the given PCB.

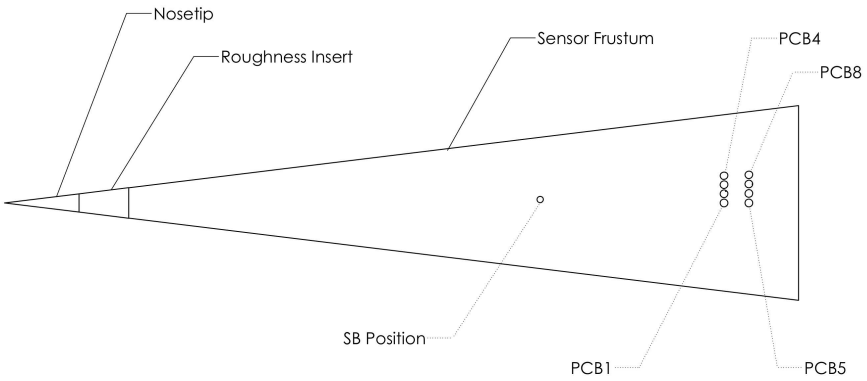

(a) The McKenzie-Ward cone, used initially to measure secondary instabilities near the aft of the model.

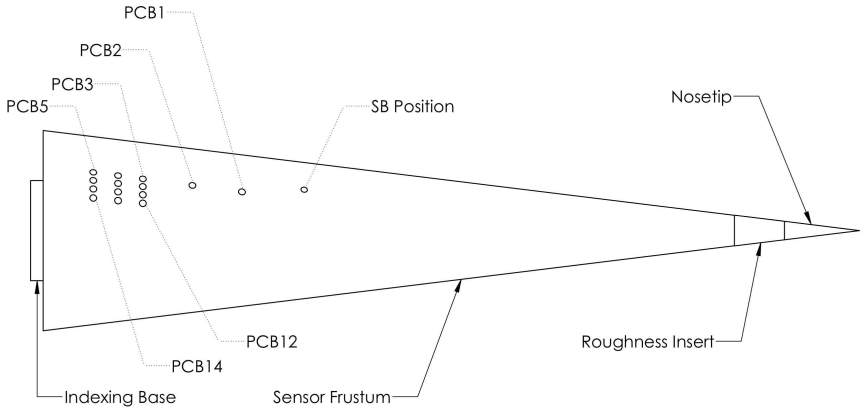

(b) The Streamline cone, used to measure secondary instability growth along a stationary vortex.

Figure 14. Schematics of the models used in the present experiment.

C. Secondary Instability Measurements

In low-speed flows, secondary instabilities of the stationary crossflow wave can generally be classified as either type-I or type-II modes,[10] with type-II modes roughly double the frequency of type-I.[11] Type-I modes are formed in regions of strong shear in the θ-direction, whereas type-II modes form in regions of high r-direction shear. Craig and Saric suggest an estimate for the frequency of each mode is $f_I \approx U_e/(2\delta)$ and $f_{II} \approx U_e/\delta$, respectively.[11] Note that the type-I estimation is the same as for second mode waves.[6] For the present experiment, the frequency was estimated using the US3D CFD data for the edge velocity and boundary layer thickness at the azimuthal location of the PCB in question. The CFD data is for a single unit Reynolds number and stagnation temperature, about 11×10^6 m^{-1} and 435 K, respectively. To convert the estimate for the conditions of each run, the edge velocity and boundary layer thicknesses were scaled as

$$U_{e,run} \approx U_{e,CFD}\sqrt{\frac{T_{0,run}}{T_{0,CFD}}}, \tag{1}$$

$$\delta_{run} \approx \delta_{CFD}\sqrt{\frac{Re_{\infty,CFD}}{Re_{\infty,run}}}. \quad (2)$$

The estimated frequencies presented here use CFD data from a single axial location, 0.37 m from the nosetip. The estimated frequency was found to be at most 50 kHz higher (at 120° from windward) at the most upstream PCB on the Streamline cone than the most downstream PCB, along the same ray. Thus the given estimate is expected to be slightly lower than the true estimate for upstream PCBs and higher for downstream PCBs, but well within 50 kHz for the data presented in this paper.

1. *Effect of Reynolds Number Changes*

Instabilities were identified in many of the nearly 90 runs with the MW and Streamline cones, over a range of azimuthal angles from 115° to 160°. Two instabilities were measured over a wide range of Reynolds numbers from first appearance to turbulent breakdown. The power spectra and coherences of these instabilities are presented in Figures 15 and 17.

The heat transfer map in Figure 16 shows the streak which produced the instability in Figure 15 passing over the upstream sensor (PCB 1) and the downstream sensor (PCB 5). The instability was measured on the MW cone over a Reynolds number range of 1×10^6 based on the axial location of the upstream PCB row. These measurements represent five separate runs. The PCB in question was at an azimuthal angle of about 132° from the windward ray.

Three frequency peaks are evident in the power spectrum. The lowest frequency, at about 50 kHz, is the travelling crossflow wave. The largest peak, at about 200-350 kHz, is believed to be a type-II secondary instability. A third peak at 550 kHz, present only for the higher Reynolds numbers, could be a harmonic of the type-II peak, or could be another mode. The dots on the power spectrum are the estimated frequency of the type-II secondary instability, $f_{II} \approx U_e/\delta$. They are within about 50 kHz of the measured peak and show the same Reynolds number trend.

The coherences in Figure 15(b) are taken between the upstream PCB and the sensor directly downstream. At the lowest Reynolds numbers the coherence is very high, with a maximum around 0.9. As the secondary instability develops, the coherence drops and narrows, until it reaches essentially zero at the near-turbulent condition. This effect is less pronounced on the travelling wave frequency. In addition, there appears to be no coherence between the two sensors for the high frequency peak.

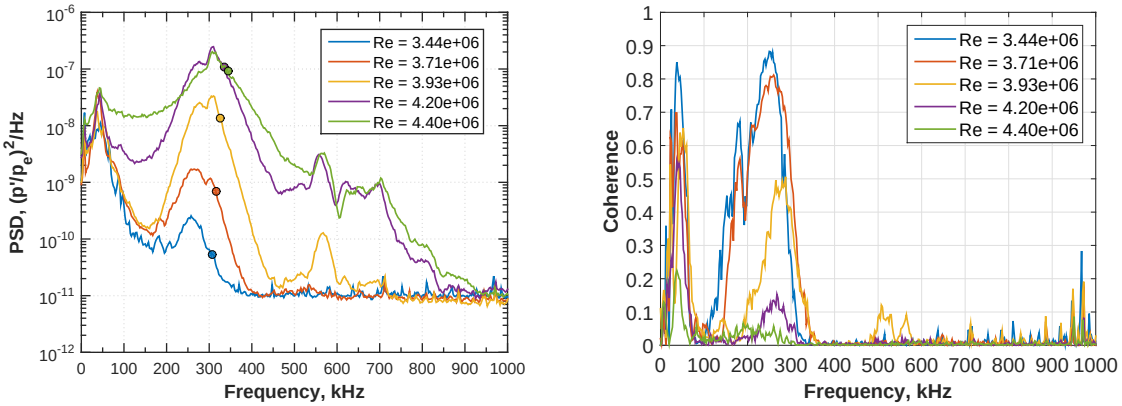

(a) Power spectra of the upstream PCB.

(b) Coherence between the two PCBs.

Figure 15. Power spectra of a secondary instability from an upstream PCB on the MW cone, and the coherence between the upstream sensor and its paired downstream PCB. Azimuthal angle $\phi = 132°$. The Reynolds numbers listed are for the upstream PCB location. The dots are the estimated frequency location.

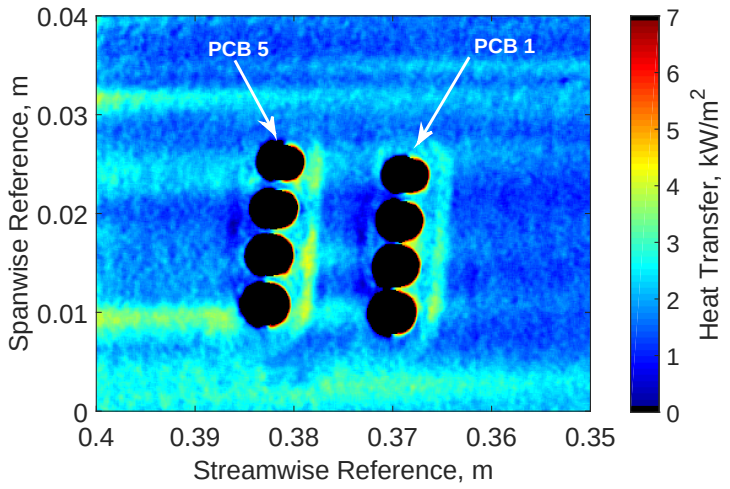

Figure 16. TSP-calculated heat transfer showing the streak which produced the instability in Figure 15. The arrows show the upstream and downstream sensors. Flow is from right to left.

The instability in Figure 17 was measured over a Reynolds number range of 2×10^6. The given PCB was at 157° from the windward ray. A heat transfer image of the streak carrying this instability is provided in Figure 18. Note that the magnitude of the heat transfer in this image may be significantly off due to issues with the reference thermocouple measurements, but the relative values are still illustrative. In the case of Figures 18 and 17, the upstream sensor is PCB 4 and the downstream sensor is PCB 8.

The power spectra in this case show the same development trends as in Figure 15(a). Again, each measurement is from a separate run. The secondary instability peak is at roughly 150 kHz. As the Reynolds number increases, the frequency shifts slightly higher, which is well tracked by the estimated type-II frequency, plotted as the colored circles. In this set of runs, as in those of Figure 15, there is a higher-frequency peak at around 300 kHz which could be a harmonic or a higher-frequency mode.

The coherence of this instability shows a slightly different trend to that of Figure 17(b). The maximum coherence is around 0.95. As the Reynolds number increases, the region of high coherence broadens by nearly 100 kHz, and significant coherence appears in the harmonic frequency band. The coherence level still drops with Reynolds number and approaches zero at the turbulent condition. The sharp spurious peaks in the coherence at high frequencies are due to ground looping in the closely-packed PCB array.

2. Effect of Small Rotations

Because the sensor locations are fixed relative to the cone, a rotation of the body leads to a measurement of a different portion of the boundary layer. If the measured instabilities were second mode waves, their amplitudes and frequencies would only change a small amount for small rotations of the cone. A secondary instability, however, only exists within the relatively small span of the stationary vortex. In addition, the roughness insert which generates the stationary waves is fixed relative to the body when the cone is rotated. This means that after rotation, a particular roughness element sees a different flowfield, and the vortex it generates will follow a different path. So a small rotation of the body should lead to a larger rotation of a given sensor relative to a particular streak.

Figure 19 shows the effect of small rotations, ranging from 1° to 6°, on the power spectra of four measured instabilities. The response is evidently widely varying. The instabilities shown in Figures 19(a) and (b) essentially cease to be measureable after 5° and 3° of rotation, respectively. Note that these instabilities are at very different azimuths, but show the same effect. However, the measured instability does not always disappear with rotation. In the case of Figure 19(c), there is only a slight change in amplitude, about half

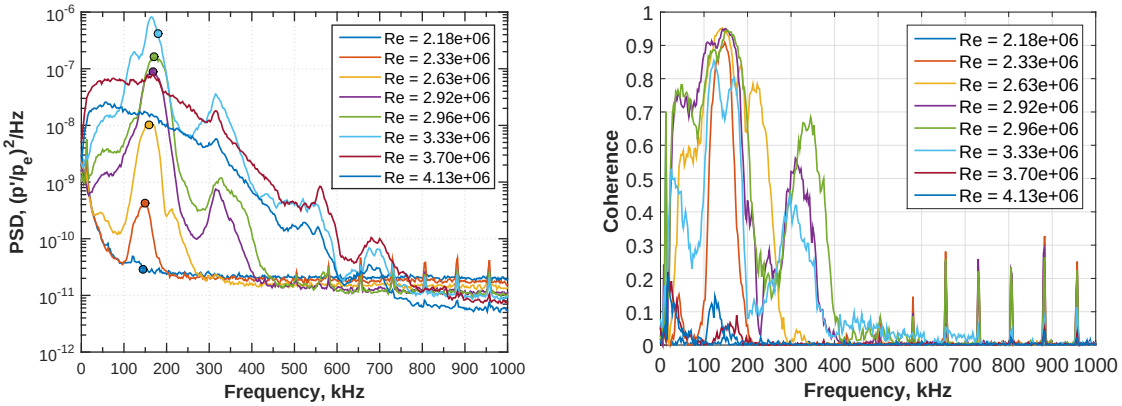

(a) Power spectra of the upstream PCB.

(b) Coherence between the two PCBs.

Figure 17. Power spectra of a different secondary instability from an upstream PCB on the MW cone, and the coherence between the upstream sensor and its paired downstream PCB. Azimuthal angle $\phi = 157°$.

an order of magnitude, and a small increase in frequency when rotated toward the lee ray, which itself is odd. In some cases for very small rotations, like 1° in Figure 19(d), what appears to be a different instability pops into existence. This phenomenon is discussed in more detail in Section D.

3. Effect of Roughness Changes

The measured instabilities appear to be sensitive to changes in the generating roughness. After the instabilities in Figures 15 and 17 were measured, the roughness insert was replaced with a smooth insert. The smooth insert results are plotted in Figure 20. In both cases there is at least an order of magnitude reduction in the instability magnitude. However, the frequencies measured in the smooth cases are not the same instabilities as those in the rough cases. Vortices will still be generated, though because the insert is smooth the vortices will be caused by random roughness on the insert or cone, or the step between the two components. A second-mode wave would not be sensitive to these changes in roughness, so the changes shown in Figure 20 indicate the measured instability is not the second mode.

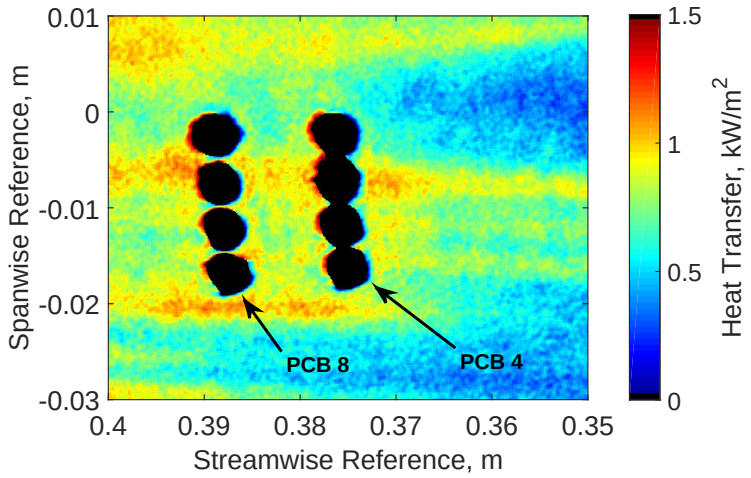

Figure 18. TSP-calculated heat transfer showing the streak which produced the instability in Figure 17. The arrows show the upstream and downstream sensors. Flow is from right to left.

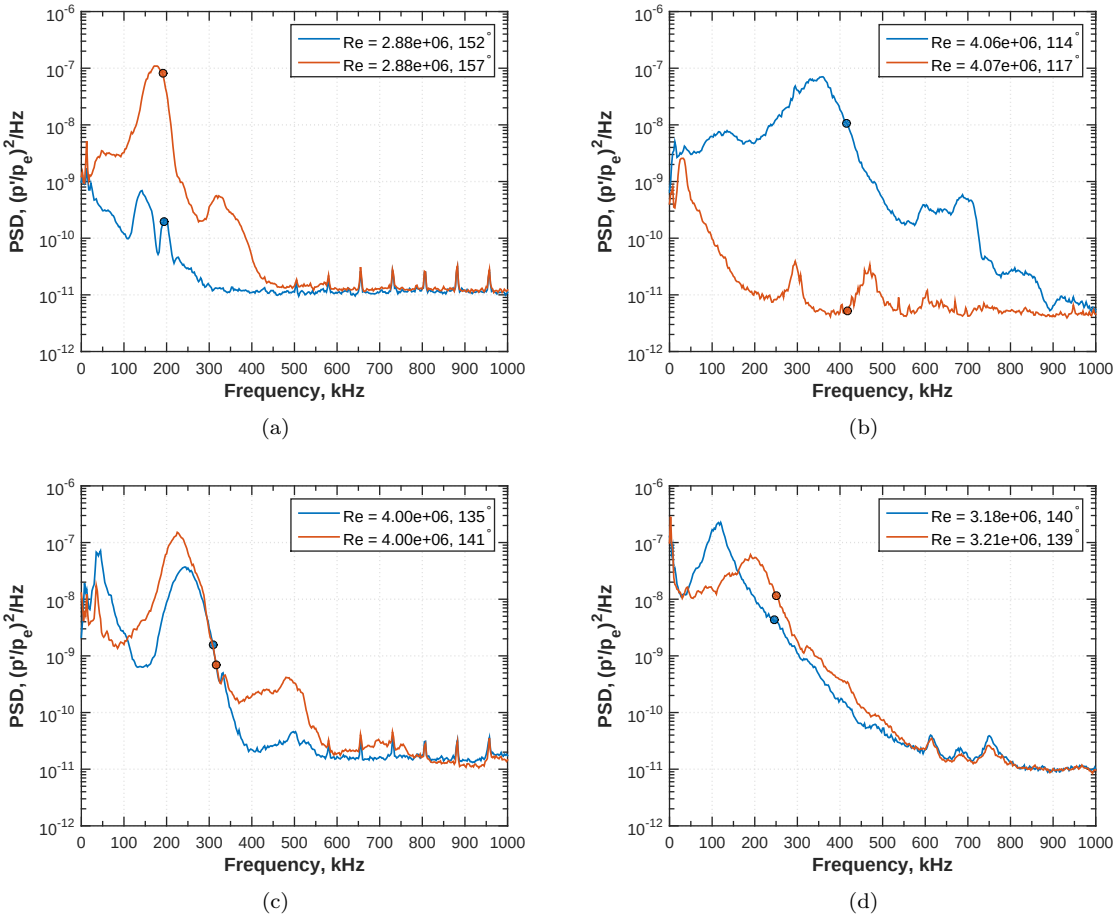

Figure 19. Power spectra of four instabilities before and after rotation of the cone. Cases (a),(c),(d) are from the MW cone, case (b) is from the Streamline cone.

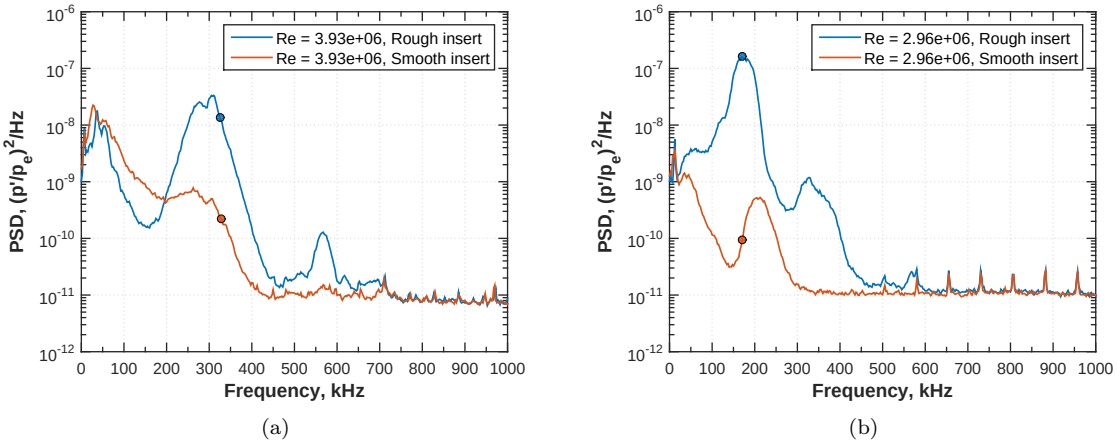

Figure 20. Power spectra for the two instabilities in Figures 15 and 17 with both a rough insert and a smooth insert.

D. Evidence of Multiple Modes of the Secondary Instability

Figure 21 is a heat-transfer image of a run using the Streamline cone. At this condition, the angle of the PCB array is slightly shallower than the angle of the stationary vortex, so the PCB array measures not only along the streak but also across it. The upstream PCBs, 1 and 2, are on the lee side of the streak. The type-I instability is expected to be on the lee side of the streak in strong ρU gradients in the θ-direction, if present.[11] The downstream PCBs, 3-5, pass into the central region of the streak where type-II instability is expected in the strong ρU gradients in the r-direction.

The power spectra provided in Figure 22 appear to confirm these expectations. The colored circles represent the type-II frequency estimate. The spectra of the upstream PCBs in Figure 22(a) show peaks at around 140 kHz, slightly more than half the type-II estimate, while the downstream PCBs in Figure 22(b) have peaks at around 225 kHz, just above the type-II estimate. A third peak appears in the downstream PCBs at around 450 kHz, which could be a harmonic or a different mode. These frequencies generally agree with the results of Craig and Saric,[11] who detected frequency content in the [80,130] kHz band on the lee side of their vortices. The higher frequency modes are above the bandwidth of their hot-wire.

Figure 23 shows the coherence between successive sensors. In Figure 23(a), PCBs 1 and 2 show strong coherence at the lower, type-I frequency band. Moving farther down and across the streak, PCBs 2 and 3 measure both instabilities, as illustrated in 23(b). Farther PCBs cease to measure a coherent wave in the type-I band, but there is strong coherence in both the type-II band and the higher frequency of unknown character.

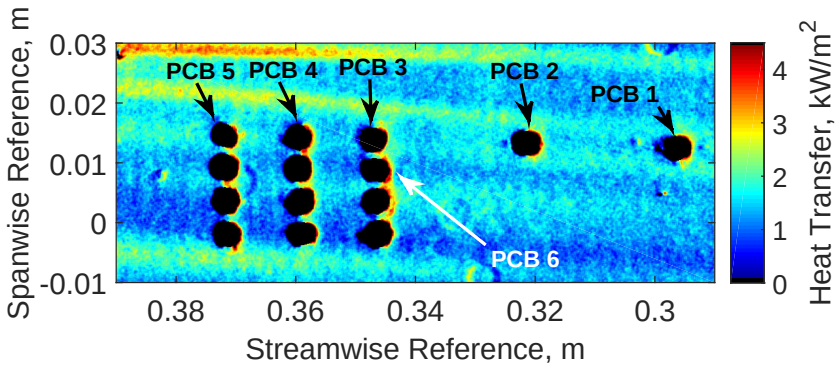

Figure 21. TSP-calculated heat transfer of the condition in Figure 22. Flow is from right to left.

E. Properties of the Secondary Instability

1. *Instability Frequencies*

As discussed in section C, CFD data were used to estimate the type-I and type-II secondary instability frequencies for the conditions of each run. The CFD data were calculated at a high Reynolds number and stagnation temperature compared to most of the actual runs, so they represent an upper bound on the type-I and type-II frequency estimates. Figure 24 shows these two curves superimposed on 55 measured frequencies from 15 different runs. Most of the measured frequencies fall within the type-I/type-II envelope. There are a few high-frequency outliers, which remain to be explained. Note that these points represent the most prominent frequency for a given PCB measurement, so potential harmonics like the high-frequency peaks in Figures 15, 17 and 22(b) are not shown.

There is considerable spread in the data. Some of the variance can be explained by differences in run conditions and PCB location. Using equations 1 and 2, the type-I and type-II estimates can be scaled. Figure 25(a) shows the scaled CFD estimate for $Re_\infty = 8\times10^6$ m^{-1} and measured data within 0.5×10^6 m^{-1}. Figure

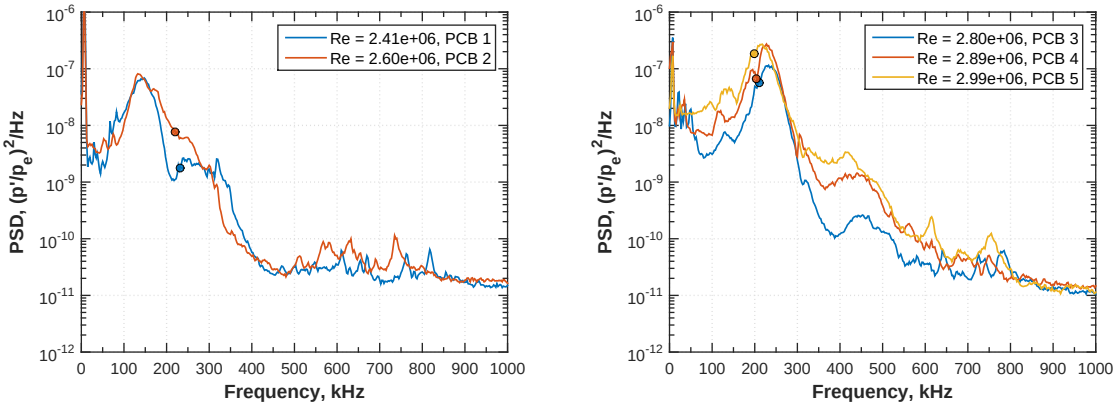

(a) Spectra for PCBs 1 and 2.

(b) Spectra for PCBs 3 - 5.

Figure 22. Power spectra of multiple instabilities under a single streak.

25(b) shows the estimate and data for runs around $Re_\infty = 11 \times 10^6$ m^{-1}. Many of the points lie close to the estimate, but there is still considerable variance, more so at higher Reynolds numbers. It is unclear what is responsible, though the model temperature and PCB axial location have an effect and are unaccounted for. In addition, the scaling of the CFD data with Reynolds number and stagnation temperature is not entirely accurate. The high frequency points above the type-II estimate (350 kHz in 25(a), 450 kHz in 25(b)) may be a third mode of the secondary instability. Figure 25 also gives an idea of the Reynolds number ranges which yield secondary instabilities at different azimuthal locations.

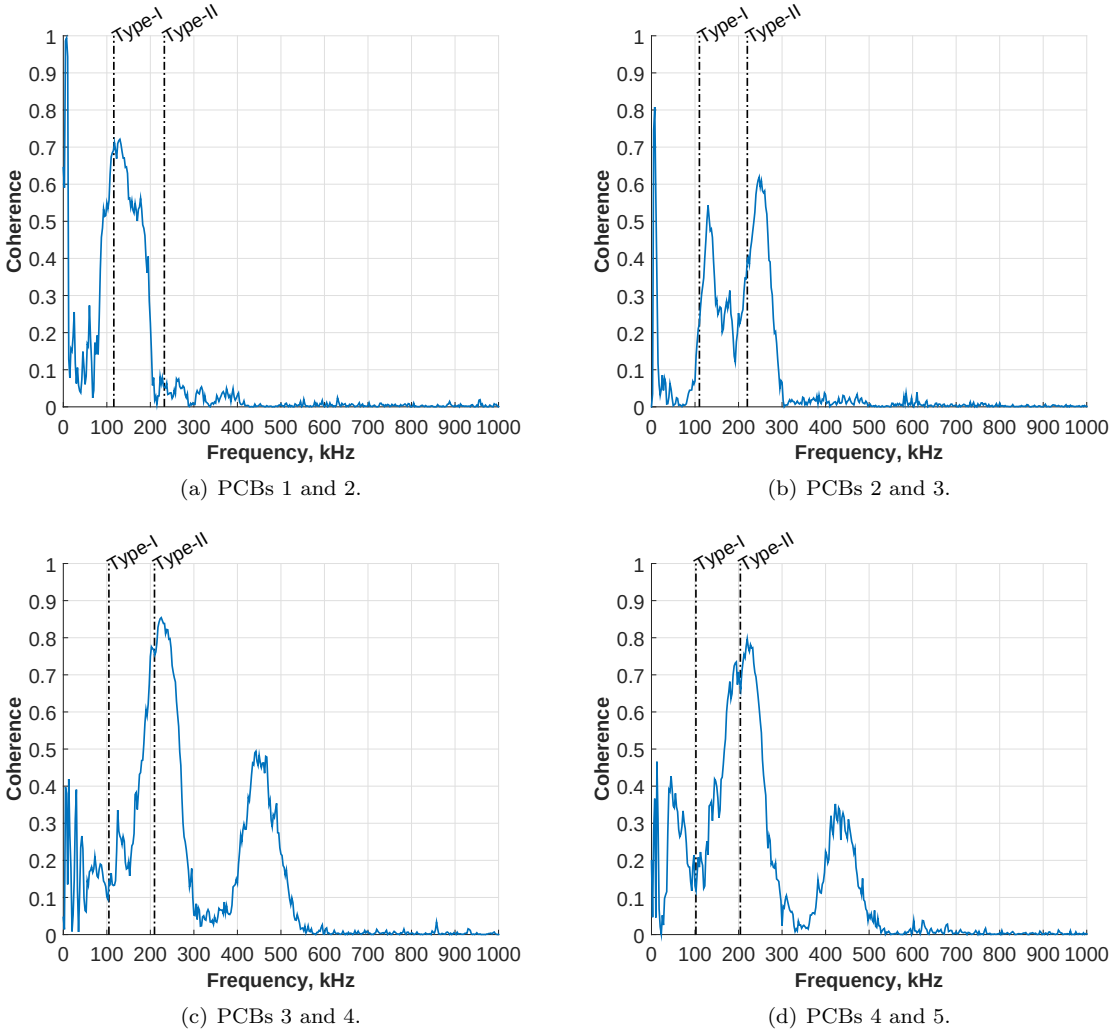

(a) PCBs 1 and 2.

(b) PCBs 2 and 3.

(c) PCBs 3 and 4.

(d) PCBs 4 and 5.

Figure 23. Coherence between successive PCBs for the instability in Figure 22.

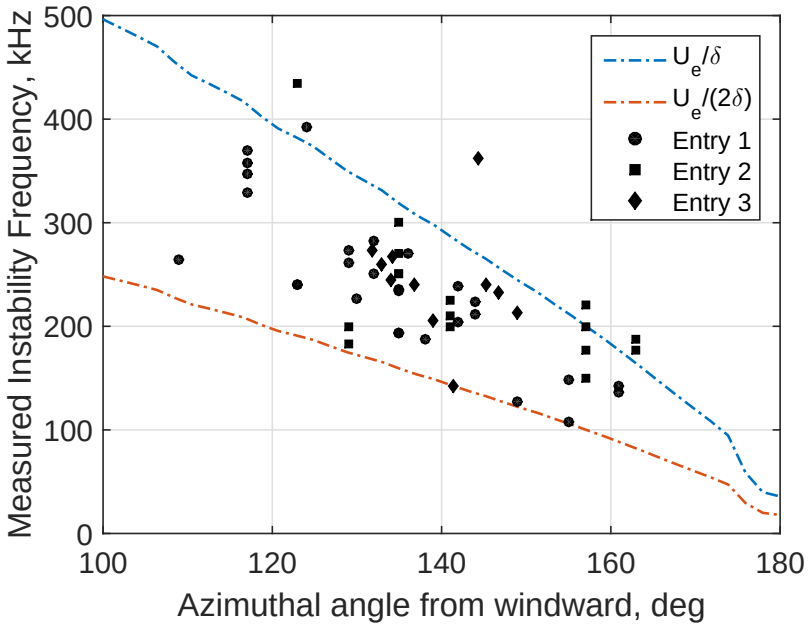

Figure 24. A plot of 55 measured instability frequencies from 15 different runs. The dashed lines are the type-I and type-II frequency estimates for $Re_\infty = 11 \times 10^6$ m^{-1} and $T_0 = 435$ K. Shapes are different entries.

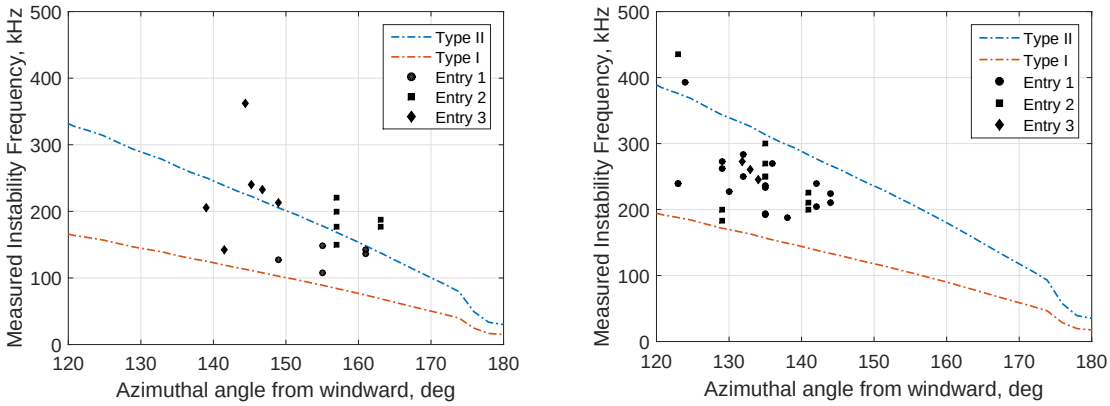

(a) Runs with $Re_\infty \approx 8 \times 10^6$ m^{-1}.

(b) Runs with $Re_\infty \approx 11 \times 10^6$ m^{-1}.

Figure 25. A plot of measured instability frequencies at unit Reynolds numbers within 0.5 million of 8 (a) and 11 (b) million per meter. The dashed lines are the type-I and type-II CFD-based frequency estimates scaled to this condition.

2. Wave Speeds

Because the secondary instability rides the stationary vortex, two sensors along the vortex are sufficient to calculate the wave speed of the instability. The group delay of the waves can be calculated as $\tau_g = (d\Theta/df)/2\pi$, where $\Theta(f)$ is the phase of the cross power spectral density. Table 1 shows the wave speeds for the instabilities presented in Figures 15, 17, and 22, as well as a few others. The wave speeds were calculated in the frequency band where the coherence is greater than 0.4. In this band, the phase function $\Theta(f)$ was fit with a line whose slope is the group delay. The group velocity is then the distance between the two sensors divided by the delay. The wave speeds are all close to the edge velocity, regardless of azimuthal orientation or frequency band.

Table 1. Group wave speeds for several instabilities.

Frequency Band, kHz	Azimuthal Angle, deg	Average Group Speed, c/U_e
168 - 307	132	0.98^{*}
253 - 302	132	1.23^{*}
108 - 175	157	1.08^{**}
20 - 200	157	0.94^{**}
85 - 198	131	$0.99^{\dagger}$
173 - 272	137	$1.12^{\dagger}$
200 - 307	144	1.16
35 - 222	163	1.01

* instability in Figure 15
** instability in Figure 17
† instability in Figure 22

3. Amplitude Growth

For the two cases presented which show the nearly full development of the instability, a calculation of instability amplitudes and growth factors may aid in the development of a more robust transition predictor. The amplitudes were calculated for a 200 kHz bandwidth centered on the secondary instability peak and a 100 kHz bandwidth centered on the higher-frequency peak. Figure 26(a) shows the calculated amplitudes of the instability in Figure 15 for both the upstream and downstream sensors. Five times during each run were examined; each run is denoted by a different color in the Figure. In general the amplitudes are close, but the upstream fluctuations become larger at higher Reynolds numbers. The reason for this divergence is unclear. The peak amplitude is between 10%-16% of the edge pressure. Figure 26(b) compares the 'primary' instability to the higher-frequency instability, for the upstream sensor. The higher-frequency amplitudes are about eight times smaller.

Figure 27(a) shows the amplitudes of the instability in Figure 17, for both the upstream and downstream sensor. In this case, the divergence between the two sensors still exists at higher Re but is much less pronounced. In addition, a much wider range of the development has been captured, from first appearance to turbulence. The amplitude development is peaky, with the peak occurring shortly before turbulence. The peak fluctuations are between 19% and 24% of the edge pressure, significantly higher than in Figure 26. Figure 27(b) compares the 'primary' instability to the high frequency peak at the upstream sensor. They show similar developments, with the high-frequency amplitudes roughly four times smaller than the 'primary'.

The amplitude growth factor $\ln(A/A_0)$ of the upstream sensors is provided in Figure 28. Because the initial amplitudes of the instabilities are unknown, the data are normalized by the lowest recorded amplitude for each sensor. These normalization amplitudes are listed in table 2. The data from Figure 26 is shown in Figure 28(a). Here the maximum growth factor before transition is roughly 3.75 for the primary instability

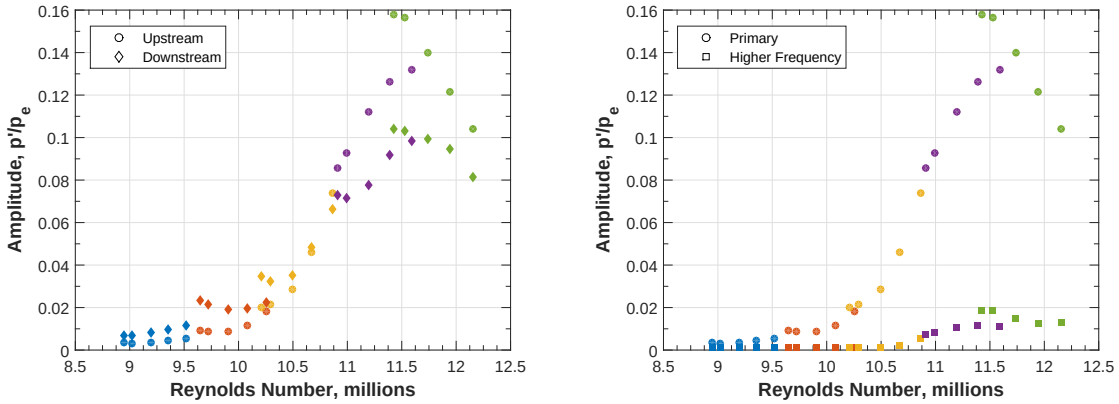

(a) (b)

Figure 26. Instability amplitude development for the case of Figure 15. The 'primary' frequency is in the range 200-400 kHz, the 'high frequency' instability is around 500-600 kHz.

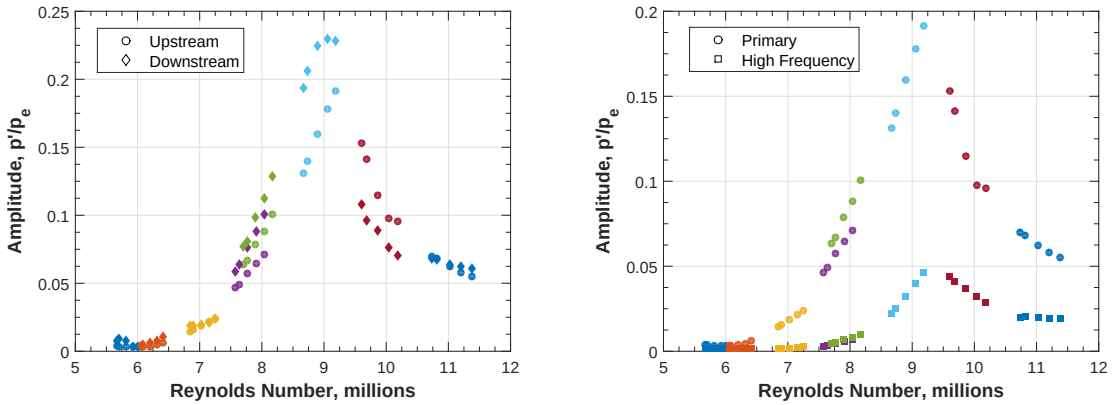

(a) (b)

Figure 27. Instability amplitude development for the case of Figure 17.

and 2.5-3 for the high-frequency instability. For the instability in Figure 28(b) (from Figure 27), the peak growth factor is about 4 for the primary and about 3.5 for the high-frequency instability. Note that these two instabilities were recorded far apart azimuthally, at 132° and 157°, yet still have very similar peak growth factors.

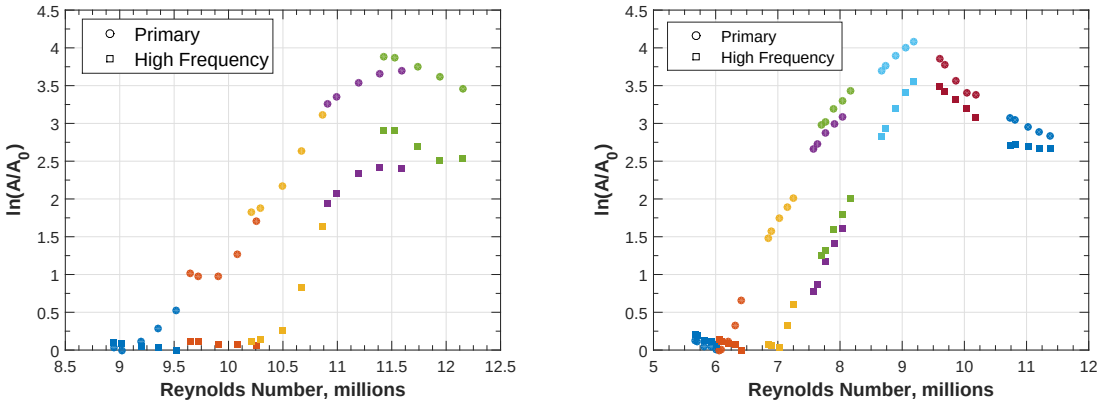

(a) From Figure 26 data.

(b) From Figure 27 data.

Figure 28. Calculated growth factors for the primary and high-frequency peaks of two instabilities.

Table 2. Amplitudes used for normalizing the data in Figure 28.

Dataset	Lowest Measured Amplitude A_0, %
Figure 28(a), primary	0.33
Figure 28(a), high frequency	0.10
Figure 28(b), primary	0.32
Figure 28(b), high frequency	0.13

IV. Conclusion

1. Using a RIM roughness insert with 30 evenly spaced elements, experiments were performed to determine the effect of decreasing the height of the roughness elements on the second-mode instability on a flared cone geometry. Heights ranging from 0.020" down to 0.006" were tested, and it was observed that as the height decreased the magnitude of the pressure fluctuations increased to nearly 25%. Additionally, an adjustable angle-of-attack adapter was tested and showed improvement in obtaining a 0° angle of attack when using the flared cone model.Future tests with the adjustable angle-of-attack adapter will allow for improved axisymmetric comparisons of the flowfield around the flared cone.

2. The measured instabilities coincide with stationary vortices visible in TSP imaging, and appear to have a small spatial footprint as illustrated by the rotation data. In addition, they are sensitive to the magnitude of roughness near the nose of the cone. This is all evidence that the measured instabilities are not second mode waves or travelling waves but are in fact secondary instabilities of the hypersonic stationary crossflow wave. Finally, the frequencies of the measured instabilities are either at the expected second-mode frequency or more commonly roughly double or quadruple it, much higher than typical travelling wave frequencies. These frequencies correspond well to the estimated type-I and type-II modes of the secondary instability as studied at low speeds.

V. Acknowledgements

This research is funded by the Air Force Office of Scientific Research under grant number FA9550-12-1-0167. Heath Johnson and Graham Candler at the University of Minnesota were very helpful in installing STABL on our Purdue computer and for their assistance in running the code.

References

[1]Schneider, S. P., "Developing Mechanism-Based Methods for Estimating Hypersonic Boundary-Layer Transition in Flight: The Role of Quiet Tunnels," *Progress in Aerospace Sciences*, Vol. 72, January 2015, pp. 17–29.

[2]Schneider, S. P., "Laminar-Turbulent Transition on Reentry Capsules and Planetary Probes," *AIAA-2005-4763*, June 2005.

[3]Steen, L. E., *Characterization and Development of Nozzles for a Hypersonic Quiet Wind Tunnel*, Master's thesis, Purdue University, School of Aeronautics and Astronautics, December 2010.

[4]Wheaton, B. M., "Boundary Layer Stability on Circular-Arc Geometries at Mach 6," Tech. rep., Purdue University AAE 624 Final Report, December 2008.

[5]Chynoweth, B., Ward, C., Henderson, R., Moraru, C., Greenwood, R., Abney, A., and Schneider, S., "Transition and Instability Measurements in a Mach 6 Hypersonic Quiet Wind Tunnel," AIAA Paper 2014-0074, January 2014.

[6]Chynoweth, B. C., *A New Roughness Array for Controlling the Nonlinear Breakdown of Second-Mode Waves at Mach 6*, Master's thesis, Purdue University, School of Aeronautics and Astronautics, August 2015.

[7]Willems, S., Gülhan, A., Ward, C. A., and Schneider, S. P., "Free Transition on a Slender Cone in a Quiet and a Conventional Wind Tunnel and the Effect of Ultrasonically Absorptive Materials," Presented at the 6th European Conference for Aeronautics and Space Sciences, June-July 2015.

[8]Malik, M. R., Li, F., and Chang, C.-L., "Nonlinear Crossflow Disturbances and Secondary Instabilities in Swept-Wing Boundary Layers," *IUTAM Symposium on Nonlinear Instability and Transition in Three-Dimensional Boundary Layers*, edited by P. W. Duck and P. Hall, 1996, pp. 257–266.

[9]Malik, M. R., Li, F., Choudhari, M. M., and Chang, C.-L., "Secondary Instability of Crossflow Vortices and Swept-Wing Boundary-Layer Transition," *Journal of Fluid Mechanics*, Vol. 399, 1999, pp. 85–115.

[10]White, E. B. and Saric, W. S., "Secondary Instability of Crossflow Vortices," *Journal of Fluid Mechanics*, Vol. 525, 2005, pp. 275–308.

[11]Craig, S. A. and Saric, W. S., "Experimental Study of Crossflow Instability on a Mach 6 Yawed Cone," AIAA 2015-2774, June 2015.

[12]Ward, C. A. C., Henderson, R. O., and Schneider, S. P., "Possible Secondary Instability of Stationary Crossflow Vortices on an Inclined Cone at Mach 6," AIAA 2015-2773, June 2015.

[13]McKiernan, G. R., Chynoweth, B. C., Edelman, J. B., McKenzie, J. A., Sweeney, C. J., and Schneider, S. P., "Instability and Transition Experiments in the Boeing/AFOSR Mach 6 Quiet Tunnel," AIAA 2015-2317, June 2015.